Finite Su-Schrieffer-Heeger chains coupled to a two-level emitter: Hybridization of edge and emitter states

C. I. Kvande [1,2,3] D. B. Hill [1,2] and D. Blume [1,2]

[1]*Homer L. Dodge Department of Physics and Astronomy, The University of Oklahoma,*
440 W. Brooks Street, Norman, Oklahoma 73019, USA

[2]*Center for Quantum Research and Technology, The University of Oklahoma, 440 W. Brooks Street, Norman, Oklahoma 73019, USA*

[3]*Physics Department, Kalamazoo College, 1200 Academy Street, Kalamazoo, Michigan 49006, USA*

The Hamiltonian for the one-dimensional Su-Schrieffer-Heeger (SSH) chain is one of the simplest Hamiltonians that supports topological states. This work considers between one and three finite SSH chains with open boundary conditions that either share a lattice site (or cavity), which—in turn—is coupled to a two-level emitter, or are coupled to the same two-level emitter. We investigate the system properties as functions of the emitter-cavity coupling strength g and the detuning between the emitter energy and the center of the band gap. It is found that the energy scale introduced by the edge states that are supported by the uncoupled finite SSH chains leads to a g-dependent hybridization of the emitter and edge states that is unique to finite-chain systems. A highly accurate analytical three-state model that captures the band-gap physics of k-chain ($k \geqslant 1$) systems is developed. To quantify the robustness of the topological system characteristics, the inverse participation ratio for the cavity-shared and emitter-shared systems consisting of k chains is analyzed as a function of the on-site disorder strength. The g-dependent hybridization of the emitter and uncoupled edge states can be probed dynamically.

I. INTRODUCTION

The study of individual photons confined in a reflective cavity interacting with matter, frequently a few-level emitter (e.g., an atom), is at the heart of many quantum studies [1–5]. Chief accomplishments in the field of cavity quantum electrodynamics (QED), such as the manipulation of atoms through photons and, conversely, the manipulation of individual photons by atoms, were recognized by the 2012 Nobel Prize for physics [6,7]. An important extension of cavity QED is waveguide QED, where the cavity is replaced by a one-dimensional radiation channel or waveguide [8–15]. The one-dimensional waveguide confines the photons, which interact with one or more quantum emitters that are localized at specific positions along the waveguide. Such systems can feature hybridized bound and propagating light-emitter states as well as super- and subradiance and play a central role in various quantum information processing protocols [16–19]. In dissipation engineering protocols, the waveguide serves as a highly tunable nontrivial reservoir [20–22].

The interplay between a topological waveguide QED bath and one or more localized two-level emitters (2LEs) was investigated in a seminal paper by Bello *et al.* [12]. It was found that the coupling of a 2LE to a photonic bath with periodic boundary conditions (BCs) described by the Su-Schrieffer-Heeger (SSH) Hamiltonian gives rise to a chiral zero-energy bound state if the emitter's frequency is tuned to lie in the middle of the band gap of the bath dispersion. The SSH model was originally introduced to describe solitons in polyacetylene [23] and has been used extensively as an analytically tractable model for topological investigations [24–27]. The SSH bath consists of two sublattices (sublattice 1 and sublattice 2; see Fig. 1) with interunit hopping energy v and intraunit hopping energy u. For $|v| > |u|$, the zero-energy chiral bound state supported by the emitter-chiral waveguide Hamiltonian with the emitter tuned to be in resonance with the middle of the band gap was found to have the following characteristics for all emitter-cavity coupling strengths g [12,28]:

(i) The photonic component of the bound state has only a finite amplitude in the sublattice that the two-level emitter does not couple to (in our case, the emitter couples to sublattice 1 of unit cell n^*, implying that the photonic component occupies sublattice 2).

(ii) The photonic component of the bound state occupies only the side of the chain where the cavity of sublattice 2 of the unit cell adjacent to unit cell n^* is connected to the cavity of sublattice 1 of the unit cell n^* via a strong bond (left arm in Fig. 1).

(iii) The bound state inherits the properties of the topological edge state; e.g., it is robust against disorder.

This work considers a *finite* SSH chain with open BCs coupled to a 2LE. Without the 2LE, the SSH Hamiltonian with open BCs supports two topologically protected edge states that live in the band gap. Building on the work presented in the supplemental material of Bello *et al.* [12], the system properties are analyzed as functions of the emitter-bath coupling strength g and the emitter frequency, focusing on parameter combinations for which the hybridization between the emitter and the edge states plays a prominent role. The finite waveguide with open BCs and zero detuning supports, as the corresponding system with periodic BCs, a zero-energy
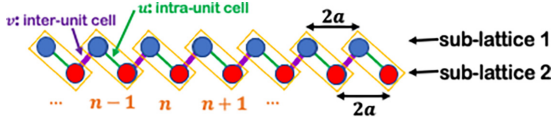
FIG. 1. Illustration of the SSH chain. Each unit cell, marked by an orange box and labeled by n, contains a cavity that belongs to sublattice 1 (solid blue circle) and a cavity that belongs to sublattice 2 (solid red circle). The intraunit and interunit hopping energies are denoted by u and v, respectively. The spacing between neighboring unit cells is $2a$.

state. The photonic contribution of this state has its maximum at a cavity located at the edges of the chain as opposed to, as found for periodic BCs, at a cavity that sits next to the cavity that the emitter is coupled to. For g larger than a value that depends on the edge energy of the finite SSH chain and the emitter location on the chain, the emitter contribution to the chiral zero-energy state is essentially zero. The emitter instead hybridizes with the two $g = 0$ edge states, resulting in two finite-energy states that play the role of edge states in the arm of the chain that is not occupied by the chiral zero-energy state. A simple analytical three-state model that captures the behaviors for both vanishing and nonvanishing detuning is presented.

Motivated by the possibility that cavities can be connected in nontrivial geometries, we extend our studies to two and three "crossed chains" that are connected either by sharing a cavity or by coupling to a shared 2LE. Both scenarios can be thought of as having a single site, either the shared cavity or the shared emitter, with a coordination number that is, respectively, two and three times larger for the two-chain and three-chain scenarios than the coordination number of the other cavities. Even though the number of $g = 0$ states in the middle of the gap increases with k, we find that the g-dependent characteristics of emitter- and cavity-shared k-chain systems can be described by the same analytical three-state Hamiltonian as the one-chain system, provided the effective coupling constant is chosen accordingly. Our results extend readily to $k > 3$.

Our findings highlight that finite baths, as frequently realized experimentally, display—compared to infinite baths—distinct characteristics that are due to the new energy and length scales introduced by the finiteness of the system. In the case of the topological bath, there is not only an energy scale that emerges from the finite length of the chain (which sets, e.g., a time for photons to travel to the end of the chain and back and which also exists for nontopological chains) but also an energy scale that emerges from the splitting of the two edge states supported by the bath (this energy scale does not exist in a nontopological bath and goes to zero for a topological bath as N approaches infinity).

The remainder of this paper is organized as follows. Section II introduces the system Hamiltonians and static properties, including a discussion of the eigenspectra of k-chain systems ($k = 1$–3) and the emergence of dark states; mathematical details are relegated to Appendixes A–D. Section III investigates the robustness of the states that have topological characteristics to chiral-symmetry-breaking disorder while Sec. IV shows that the g-dependent hybridization can be probed dynamically. Section V concludes and presents an outlook.

II. HAMILTONIAN, EIGENENERGIES, AND EIGENSTATES

A. SSH Hamiltonian

For a chain that consists of N unit cells, the SSH Hamiltonian $\hat{H}_{\text{SSH}}$, which is schematically illustrated in Fig. 1, reads

$$\hat{H}_{\text{SSH}} = \sum_{n=1}^{N-1}[(u\hat{c}_{n,1}^\dagger \hat{c}_{n,2} + v\hat{c}_{n,2}^\dagger \hat{c}_{n+1,1}) + \text{H.c.}]$$
$$+ [(u\hat{c}_{N,1}^\dagger \hat{c}_{N,2} + v_N \hat{c}_{N,2}^\dagger \hat{c}_{1,1}) + \text{H.c.}], \quad (1)$$

where $\hat{c}_{n,j}$ annihilates an excitation in the jth sublattice ($j = 1$ or 2) of the nth unit cell. The parameters u and v, which are taken to be real and positive throughout this paper, denote intraunit cell and interunit cell hopping energies, respectively. Periodic and open BCs are realized for $v_N = v$ and $v_N = 0$, respectively. Throughout, we use u and $\hbar/u$ as our energy and time units. The SSH model has elucidated phenomena in many subdisciplines of physics including chemical physics [29], condensed matter physics [30], cold-atom physics [25], and relativistic field theories [31]. Throughout this paper, we have a scenario in mind where each unit cell contains two cavities (one that belongs to sublattice 1 and one that belongs to sublattice 2; see Fig. 1) and where the operators $\hat{c}_{n,j}$ and $\hat{c}_{n,j}^\dagger$ annihilate and create a photon in the cavity that belongs to sublattice j of the nth unit cell.

Since the SSH Hamiltonian possesses a chiral symmetry, it is a paradigmatic model for studying topology. Specifically, the chiral operator $\hat{C}$ and $\hat{H}_{\text{SSH}}$ anticommute, $\hat{C}\hat{H}_{\text{SSH}}\hat{C} = -\hat{H}_{\text{SSH}}$, where $\hat{C}$ is defined in terms of the projection operators $\hat{P}_j$ ($j = 1$ or 2), $\hat{C} = \hat{P}_1 - \hat{P}_2$, and $\hat{P}_j = \sum_{n=1}^{N} \hat{c}_{n,j}^\dagger \hat{c}_{n,j}$. For concreteness, we consider the setup in Fig. 1. If v is smaller than u, $\hat{H}_{\text{SSH}}$ is topologically trivial. Since the interunit hopping strength is weaker than the intraunit hopping strength, the two cavities contained in a given unit cell are "binding together"; i.e., the hopping strengths "respect" the chain's division into unit cells. If, on the other hand, v is larger than u, $\hat{H}_{\text{SSH}}$ is topologically nontrivial. In this case, a cavity from the nth unit cell and a cavity from the $(n + 1)$th unit cell are binding together, leading to interunit cell bonds. For open BCs, this leads to a single dangling or unpaired cavity on each end of the chain and the emergence of two edge states that are predominantly located at the first and Nth unit cells [32].

For later reference, we introduce approximate expressions for the edge states $|\psi_\pm^{\text{C1}}\rangle$,

$$|\psi_\pm^{\text{C1}}\rangle = \frac{1}{\sqrt{2}}\left(\left|\psi_{\text{edge,L}}^{\text{C1}}\right\rangle \pm \left|\psi_{\text{edge,R}}^{\text{C1}}\right\rangle\right), \quad (2)$$

where $|\psi_{\text{edge,L}}^{\text{C1}}\rangle$ and $|\psi_{\text{edge,R}}^{\text{C1}}\rangle$ are localized in sublattice 1 near the first unit cell and in sublattice 2 near the Nth unit cell, respectively:

$$\left|\psi_{\text{edge,L}}^{\text{C1}}\right\rangle = \sum_{n=1}^{N} c_{n,1}|n, 1\rangle \quad (3)$$

and

$$|\psi_{\text{edge,R}}^{\text{C1}}\rangle = \sum_{n=1}^{N} c_{n,2}|n, 2\rangle. \tag{4}$$

Here, the site basis states $|n, j\rangle$, where $n = 1, \ldots, N$ labels the unit cell and $j = 1, 2$ indicates the sublattice, are used. The superscript "C1" (chain 1) is introduced with a view toward the $k > 1$ discussion below. The expansion coefficients $c_{n,1}$ and $c_{n,2}$ read

$$c_{n,1} = \mathcal{N}(-1)^{n+1}(u/v)^{n-1} \tag{5}$$

and

$$c_{n,2} = \mathcal{N}(-1)^{N-n}(u/v)^{N-n}, \tag{6}$$

with $\mathcal{N}$ denoting a normalization constant,

$$\mathcal{N} = [1 - (u/v)^2]^{1/2}[1 - (u/v)^{2N}]^{-1/2}. \tag{7}$$

Equations (2)–(7) become exact in the $N \to \infty$ limit. The states $|\psi_{\pm}^{\text{C1}}\rangle$ have energy $\pm E_{\text{edge}}$, where

$$E_{\text{edge}} = (-1)^{N+1}\mathcal{N}^2(u/v)^{N-1}u. \tag{8}$$

The energy E_{edge} approaches zero exponentially with increasing N.

In the $N \to \infty$ limit, the edge states have vanishing energy and are characterized by a localization length $\zeta_{\text{loc}} = 2a/\ln(v/u)$, where $2a$ denotes the separation between neighboring unit cells [32]. For $v = 2u$, as considered throughout this paper, ζ_{loc} evaluates to $\approx 2.89a$. Moreover, if a site from sublattice 1 (sublattice 2) sits at the end of the chain, the edge state has zero amplitude in sublattice 2 (sublattice 1) at that end. Since zero-energy eigenstates are simultaneously eigenstates of $\hat{C}$, this follows directly from the chiral symmetry. Note that zero-energy eigenstates, and correspondingly edge states, are not supported for periodic BCs. Yet, the systems with open and periodic BCs are intimately related through the bulk-edge correspondence [32–34].

The blue circles in Fig. 2 show the energy spectrum, plotted as a function of the normalized eigenstate index, for a chain with open BCs, $v = 2u$, and $N = 31$. In this case, the energy $\pm E_{\text{edge}}$ of the states in the band gap is $\pm 6.98 \times 10^{-10} u$; within the digits reported, this agrees with the approximate expression (8). For comparison, the solid black line shows the eigenenergies for the infinite chain with periodic BCs. The agreement between the finite-N and infinite-N energy bands is very good. The numerically determined edge states are illustrated in the insets in the upper left and lower right of Fig. 2 using the site basis states $|n, j\rangle$. The size of the solid circles in Fig. 2 is directly proportional to the square of the amplitude of the expansion coefficients in sublattice 1 (upper row) and sublattice 2 (lower row) in the nth unit cell; the color of the circles (blue and red) represents the sign (positive and negative) of the expansion coefficients. Despite the finite number of unit cells, the eigenstates inherit the key characteristics of the thermodynamic system ($N \to \infty$ limit); i.e., the edge states have finite amplitude on just one sublattice. Moreover, the localization length of the finite-chain edge states is very close to the localization length ζ_{loc} for infinite N.
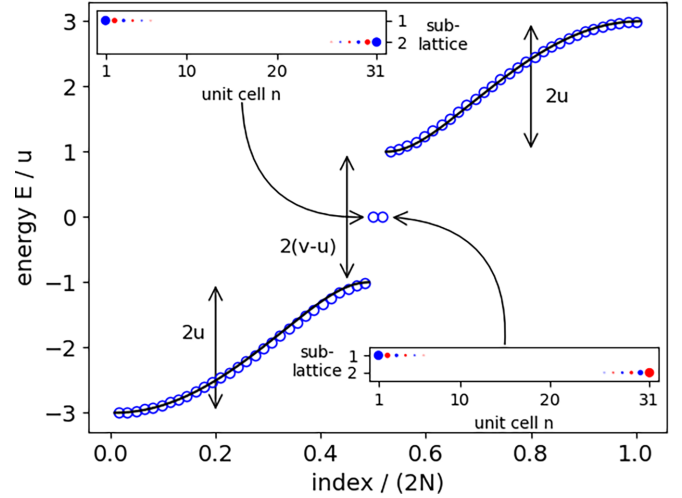

FIG. 2. Characteristics of single finite SSH chain (without the emitter) with open BCs, $N = 31$, and $v/u = 2$. The blue circles in the main panel show the eigenenergies as a function of the normalized eigenstate index. The eigenenergies are distributed symmetrically around zero energy. The spectrum features two nearly continuous energy bands and two states in the band gap with energy close to zero. The energy gap has an energy width of $2(v - u)$ while the bands each have a width of $2u$; correspondingly, the lowest and highest energy levels are separated by $2(u + v)$. For comparison, the solid black lines show the energy bands of the infinite chain with periodic BCs; the blue circles agree quite well with the solid lines. The eigenstates of the two edge states for finite N are illustrated in the upper left and the lower right insets. The size of the solid circles is directly proportional to the square of the expansion coefficient of the site basis state $|n, j\rangle$, with the color marking the sign of the expansion coefficients (see text for details).

B. Single SSH chain coupled to emitter

As alluded to in the Introduction, we are interested in k-chain systems ($k = 1$–3) coupled to a single 2LE with ground state $|g\rangle$ (energy 0) and excited state $|e\rangle$ (energy $\hbar\omega_e$). Schematics of these systems are shown in Fig. 3. This section introduces the one-chain Hamiltonian $\hat{H}_{\text{C1-2LE}}$, which is written as a sum of the SSH chain, the 2LE Hamiltonian $\hat{H}_{\text{2LE}}$, and the coupling term $\hat{H}_{\text{int}}$ (see, e.g., Ref. [8]):

$$\hat{H}_{\text{C1-2LE}} = \hat{H}_{\text{SSH}} + \hat{H}_{\text{2LE}} + \hat{H}_{\text{int}}, \tag{9}$$

$$\hat{H}_{\text{2LE}} = \frac{\hbar\omega_e}{2}(\hat{\sigma}^z + 1), \tag{10}$$

and

$$\hat{H}_{\text{int}} = g(\hat{c}_{n^*,1}^{\dagger}\hat{\sigma}^- + \hat{c}_{n^*,1}\hat{\sigma}^+). \tag{11}$$

The operators $\hat{\sigma}^z$, $\hat{\sigma}^+$, and $\hat{\sigma}^-$, which act in the Hilbert space of the 2LE, read $\hat{\sigma}^z = |e\rangle\langle e| - |g\rangle\langle g|$, $\hat{\sigma}^+ = |e\rangle\langle g|$, and $\hat{\sigma}^- = |g\rangle\langle e|$. In Eq. (11), the emitter couples, with coupling energy g ($g \geq 0$), to the cavity of sublattice 1 that belongs to the (n^*)th unit cell. In the examples considered in this work, N is odd and n^* is equal to $(N + 1)/2$. Coupling to a cavity that belongs to sublattice 2 can be treated in the same way and yields analogous results. Since Eq. (11) employs the rotating wave approximation [35], we restrict ourselves to $g/u \leqslant 0.1$ throughout this work.
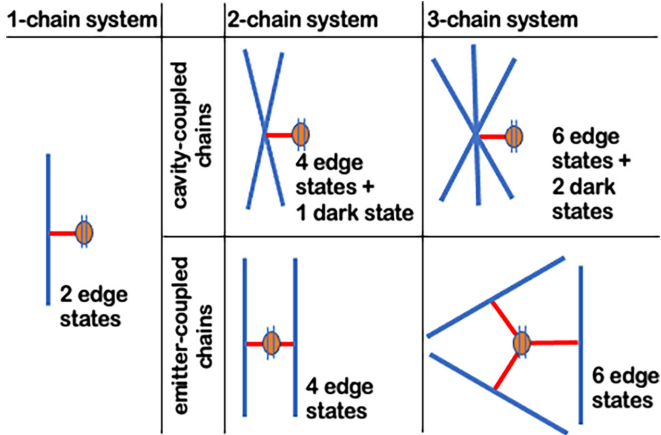
FIG. 3. Schematic of emitter- and cavity-shared k-chain systems. The blue lines represent SSH chains; from the left to the right, the number of chains increases from one to three. Each chain is coupled to an emitter (orange circle with two vertical lines). The red line represents the emitter-cavity coupling. In the emitter-shared scenario (top middle and top right panels), chains do not share cavities and one cavity of each chain is coupled to the emitter; for $g = 0$, the chains in the two- and three-chain cases are decoupled. In the cavity-shared scenario (bottom middle and bottom right panels), the two- and three-chain systems share the cavity that the emitter is coupled to. For the one-chain system, the number of sites is $2N$ (there exists no distinction between the emitter- and cavity-coupled one-chain systems). The number of sites is $4N$ and $6N$ for the emitter-shared two- and three-chain systems, respectively. The number of sites is $4N - 1$ and $6N - 2$ for the cavity-shared two- and three-chain systems, respectively. The number of edge and dark states reported next to the schematic applies to the cavity part of the Hilbert space, excluding the emitter; in the special case where the emitter detuning is zero, the coupled systems support one additional dark state (see Appendix A).

The Hamiltonian $\hat{H}_{\text{C1-2LE}}$ commutes with the excitation operator $\hat{N}_{\text{exc}}$, $\hat{N}_{\text{exc}} = \hat{P}_1 + \hat{P}_2 + |e\rangle\langle e|$, and can thus be diagonalized separately for each excitation manifold [12]. Since the dynamics discussed in Sec. IV start with the emitter in state $|e\rangle$ and the SSH chain in the zero-photon vacuum state $|\text{vac}\rangle$ (this state has $\langle\hat{N}_{\text{exc}}\rangle = 1$), we are interested in the single-excitation manifold, which is spanned by the basis states $|n, j; g\rangle$, where the first two entries refer to the SSH chain ($n = 1, \ldots, N$ and $j = 1, 2$) and the last entry refers to the emitter, and $|\text{vac}; e\rangle$. Since $\hat{C}\hat{H}_{\text{C1-2LE}}\hat{C}$ is not equal to $-\hat{H}_{\text{C1-2LE}}$, the introduction of the emitter leads to a breaking of the chiral symmetry: the emitter can be thought of as a chiral-symmetry-breaking perturbation.

Solid lines in the top row of Fig. 4 show the near-zero eigenenergies of $\hat{H}_{\text{C1-2LE}}$ as a function of the emitter energy $\hbar\omega_e$ for $v/u = 2$, $N = 15$, $n^* = 8$, and four different g/u, namely, $g/u = 10^{-4}$–10^{-1}. The spectrum is calculated using open BCs. The emitter energy can be interpreted as a detuning from the center of the band gap. For $g = 0$, the eigenstates of the three eigenenergies shown in Fig. 4 correspond to the two edge states $|\psi_-^{\text{C1}}; g\rangle$ and $|\psi_+^{\text{C1}}; g\rangle$ and the excited emitter state $|\text{vac}; e\rangle$. As the coupling g is turned on, these three states mix and the corresponding eigenenergies undergo avoided crossings. The eigenenergies that belong to the two nearly

continuous bands (not shown) and their eigenstates, in contrast, remain essentially unchanged. For small g/u, avoided crossings between two states occur when the detuning (or emitter energy) $\hbar\omega_e$ is equal to the energy $\pm E_{\text{edge}}$ of the edge states supported by $\hat{H}_{\text{SSH}}$ (for the $N = 15$ system considered in Fig. 4, $E_{\text{edge}} \approx 4.58 \times 10^{-5}u$). As expected, both avoided crossings become broader with increasing g/u. The two avoided crossings start to overlap (implying hybridization of three states) for $g/u \gtrsim 10^{-2}$. For $g/u = 0.1$, Fig. 4(d) suggests that the green and red energy levels undergo an avoided crossing, with the energy level shown in blue being decoupled and having, on the scale shown, zero energy.

Denoting the three eigenstates whose energies lie in the gap by $|\psi_l^{\text{gap}}\rangle$ ($l = 1$–3), we find that the initial state $|\text{vac}; e\rangle$ considered in the dynamical studies discussed in Sec. IV can be decomposed with good accuracy as

$$|\text{vac}; e\rangle \approx \sum_{l=1}^{3} d_l^{\text{gap}} |\psi_l^{\text{gap}}\rangle, \qquad (12)$$

where $d_l^{\text{gap}} = \langle\psi_l^{\text{gap}}|\text{vac}; e\rangle$. Solid lines in the second row of Fig. 4 show the overlap square O_l, $O_l = |\langle\text{vac}; e|\psi_l^{\text{gap}}\rangle|^2$. Since the quantity $\sum_{l=1}^{3}\mathcal{O}_l$ is greater than 0.996 for all one-chain systems considered in Fig. 4, the results presented in the second row of Fig. 4 allow us to forecast where population transfer is expected since population transfer occurs only if the initial state projects onto two or more eigenstates of the coupled system.

Since the three gap states $|\psi_l^{\text{gap}}\rangle$ can be written, with good accuracy, as a superposition of the uncoupled approximate $g = 0$ states $|\psi_-^{\text{C1}}; g\rangle$, $|\psi_+^{\text{C1}}; g\rangle$, and $|\text{vac}; e\rangle$ for all parameter combinations considered in Fig. 4, we use them to construct the three-state Hamiltonian matrix $\underline{H}_{\text{3-st.}}(G)$:

$$\underline{H}_{\text{3-st.}}(G) = \begin{pmatrix} -E_{\text{edge}} & 0 & G \\ 0 & E_{\text{edge}} & G \\ G & G & \hbar\omega_e \end{pmatrix}, \qquad (13)$$

where the effective coupling energy G is defined through $G = \langle\psi_\pm^{\text{C1}}; g|\hat{H}_{\text{int}}|\text{vac}; e\rangle$; note that G is real. Using the analytical expressions given in Eqs. (2)–(7), we find

$$G = g c_{n^*,1}/\sqrt{2}. \qquad (14)$$

While Eq. (13) is characterized by the effective coupling constant G, the three-state model introduced in the supplemental material of Ref. [12] contains both G and $-G$. Our three-state model reproduces the one-chain gap energies and overlap square data shown in Fig. 4 to 0.5% or better. Correspondingly, the model serves as a highly reliable tool for understanding the gap physics for the parameter regime of interest in this paper. Since $\hat{H}_{\text{3-st.}}(G)$ lives in the space that is spanned by states that have nonvanishing amplitude on sublattice 1 only in the left arm of the SSH chain and nonvanishing amplitude on sublattice 2 only in the right arm of the SSH chain and since it describes the gap states $|\psi_l^{\text{gap}}\rangle$ accurately, the gap states inherit chiral characteristics for all parameter combinations shown in Fig. 4.

The three-state model predicts that the hybridization of the three uncoupled basis states occurs at $|G/E_{\text{edge}}| \approx 1$ (see Appendix B). For the parameters of Fig. 4, this corresponds
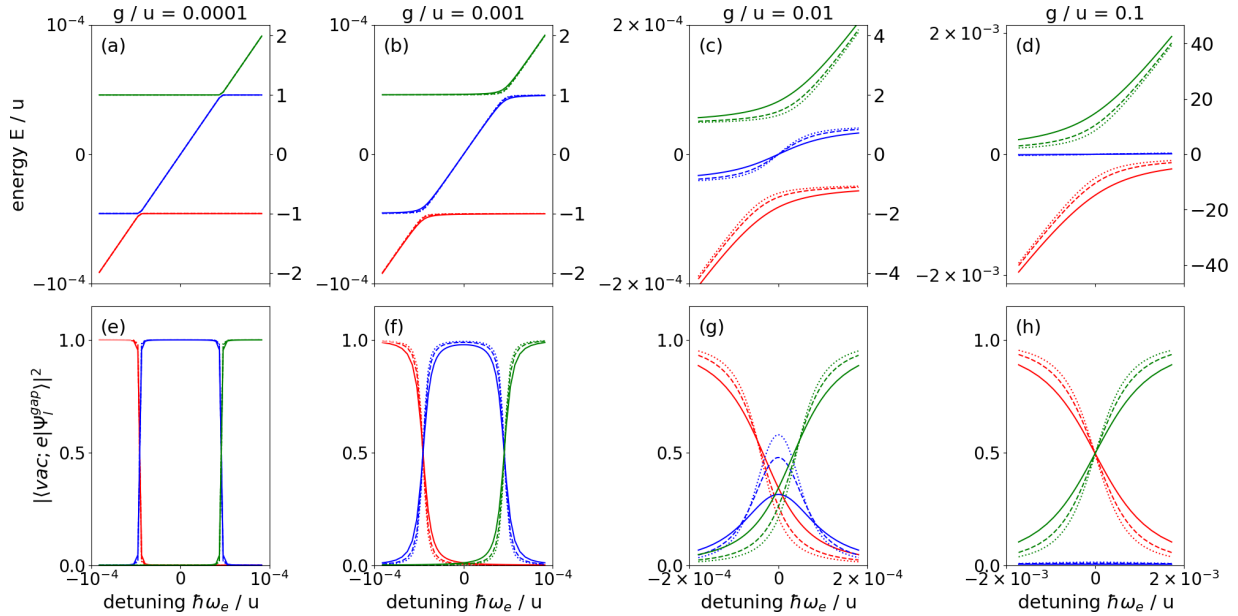
FIG. 4. Static properties of the one-chain, cavity-shared two-chain, and cavity-shared three-chain systems with open BCs, $N = 15$, $n^* = 8$, and $v/u = 2$ as a function of the detuning $\hbar\omega_e$; the figure zooms in on the physics in the vicinity of the middle of the gap. The solid, dashed, and dotted lines are for the one-chain, two-chain, and three-chain systems, respectively. The coupling g/u increases from left to right; specifically, the first, second, third, and fourth columns are for $g/u = 10^{-4}$, 10^{-3}, 10^{-2}, and 10^{-1}, respectively. The top row shows the three energy levels E_l^{gap} located in the energy gap. The left axis reports the energy in units of u (u is much larger than the typical scale of the energies in the gap) while the right axis reports the energy in units of E_{edge} ($E_{edge} \approx 4.58 \times 10^{-5}u$). The bottom row shows the overlap square $\mathcal{O}_l$. Note that the scale of the figures is the same for the first and second columns but changes for the third and fourth columns.

to $g/u \approx 10^{-2}$. For fixed u/v, the transition moves to smaller g/u with increasing N [and, as before, $n^* = (N + 1)/2$]. For fixed N and $n^* = (N + 1)/2$, the transition moves to larger g/u with decreasing v/u (keeping $v > u$).

To compare the one-chain systems with open and periodic BCs for $v/u = 2$, $N = 15$, and $n^* = 8$ (the same parameters as used in Fig. 4), we analyze the zero-energy state, which exists for $\hbar\omega_e = 0$ for both open and periodic BCs. Red solid and green dashed lines in Fig. 5 show the probability $|c_e|^2$ of the zero-energy state to be in state $|vac; e\rangle$ (approximate analytical expressions) as a function of g/u for open and periodic boundary conditions, respectively. For comparison, the symbols are obtained by diagonalizing the Hamiltonian $\hat{H}_{\text{C1-2LE}}$. The agreement between the lines and symbols is excellent. For open BCs, $|c_e|^2$ is close to 1 for small g/u and drops to a value close to zero around g/u values for which $|G/E_{edge}| \approx 1$ (arrow in Fig. 5). For periodic BCs, in contrast, $|c_e|^2$ does not decrease notably till g/u takes values of order one (or, more generally, when the coupling energy g becomes comparable to the width of the $g = 0$ energy gap). The fact that the coupling strength where the contribution $|c_e|^2$ to the zero-energy state drops significantly differs for open and periodic BCs explicitly demonstrates the role played by E_{edge}. We note that the behaviors of systems with g/u values larger than 0.1–0.5 need to be interpreted with the understanding that beyond-the-rotating-wave-approximation terms may play a non-negligible role. For small g/u, the photonic contribution to the zero-energy state of the systems with open and periodic BCs is located on different arms and localized at different positions, namely, as far away from the emitter

as possible for open BCs (see the inset in upper left corner) and on cavities close to the emitter for periodic BCs (see the inset in the middle left). The blue dotted lines and circles show $|c_e|^2$ for the nonzero energy states of the finite-chain system: $|c_e|^2$ increases relatively sharply at $|G/E_{edge}| \approx 1$. For $g/u \gtrsim 0.2$, the agreement between the numerical results and the approximate analytical expression deteriorates. This is not surprising since this is the regime where g is strong enough to couple to states that are not part of $\hat{H}_{3\text{-st.}}$. The insets in the lower right corner show the corresponding eigenstates; both have finite photonic contributions on the left arm of the chain. For finite detuning, direct comparisons between the systems with open and periodic BCs are less straightforward since the energy of the gap states (system with open BCs) and bound state (system with periodic BCs) changes differently with finite detuning.

C. Two- and three-chain systems

The cavity- and emitter-shared two- and three-chain systems are illustrated in Fig. 3. To make connections between the physics of the two- and three-chain systems and that of the single SSH chain system discussed in the previous section, we start with $g = 0$ and then consider what happens for finite g values.

The emitter-shared two- and three-chain systems reduce, for $g = 0$, to two and three independent copies of the single SSH chain. Correspondingly, the two- and three-chain systems with open BCs support a total of four and six edge states, respectively. The energy degeneracy of the edge states
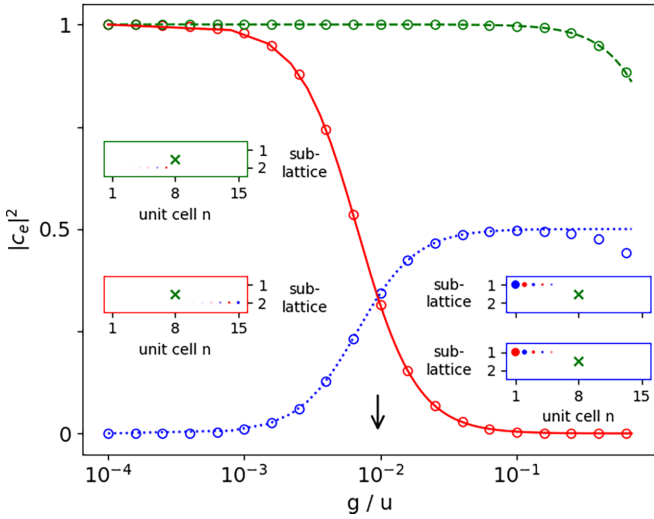
FIG. 5. Contribution $|c_e|^2$ of the state $|vac; e\rangle$ to the gap states as a function of g/u for the one-chain system with $N = 15$, $n^* = 8$, $v/u = 2$, and $\hbar\omega_e = 0$; open and periodic BCs are considered. The lines show approximate analytical results while the symbols show results obtained by diagonalizing the full Hamiltonian. The red solid line and symbols show $|c_e|^2$ of the zero-energy state for open BCs. The inset in the lower left (red box) represents the corresponding eigenstate for $g/u = 10^{-4}$. For comparison, the green dashed line and symbols show $|c_e|^2$ for the zero-energy state for periodic BCs. The inset in the upper left (green box) represents the corresponding eigenstate for $g/u = 10^{-4}$. The blue dotted line and symbols show $|c_e|^2$ of the finite-energy states for open BCs. The insets in the lower right corner (blue boxes) represent the corresponding eigenstates for $g/u = 10^{-1}$. Note that the sketches of the photonic populations for $g/u = 10^{-4}$ are, to enhance readability, multiplied by 10^6 (upper green box on the left) and 10^2 (lower red box on the left) relative to those for $g/u = 10^{-1}$. The green cross in the insets marks the unit cell that the emitter is coupled to. As a reference point, the arrow marks the coupling strength for which $|G/E_{\text{edge}}| = 1$.

is two (three) for the two-chain (three-chain) systems: For the two-chain (three-chain) systems, two (three) states have energy E_{edge} and two (three) states have energy $-E_{\text{edge}}$. Forming appropriate linear combinations of the degenerate states (see Appendix C for details), we find that four (six) of these states are, to a very good approximation, not affected by the coupling between the cavities and the emitter; i.e., their energies for finite g are approximately equal to $\pm E_{\text{edge}}$. The other three energies near zero with eigenstates $|\psi_l^{\text{gap}}\rangle$ are, as in the case of the one-chain system, very well described by a three-state model. Specifically, the three-state model discussed in the previous section applies also to the emitter-shared k-chain ($k > 1$) system, provided g is not too large and provided the effective coupling constant is replaced by $\sqrt{k}G$ (see Appendix C for details). We note also that the initial state $|vac; e\rangle$ can, to a good approximation, be expanded in terms of the three gap states $|\psi_l^{\text{gap}}\rangle$. The quantity $\sum_{l=1}^{3} \mathcal{O}_l$ is greater than 0.993 for the emitter-shared two- and three-chain systems for the parameter combinations covered in Fig. 4 (note, though, that the figure is for the cavity-shared systems).

The cavity-shared two- and three-chain systems are, even for $g = 0$, distinct from the one-chain system. Figure 6 shows
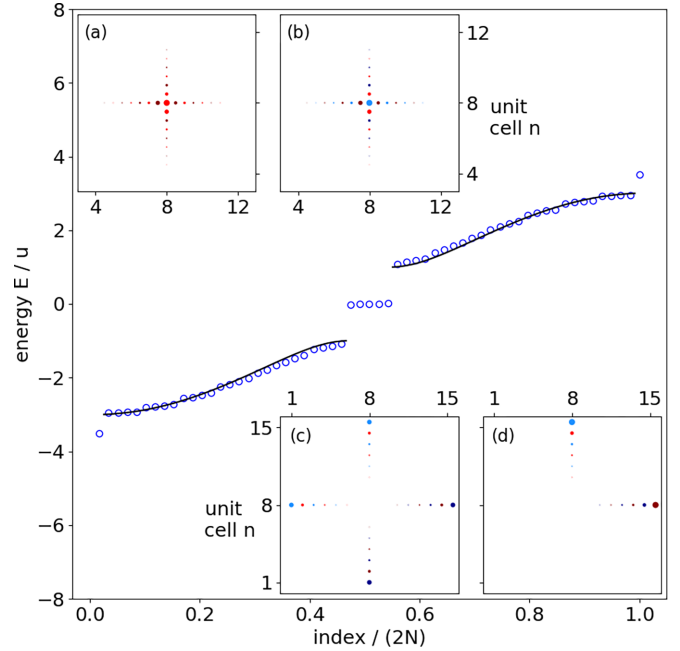

FIG. 6. Characteristics of the cavity-shared two-chain system (without the emitter) with open BCs, $N = 15$, and $v/u = 2$; the shared cavity belongs to sublattice 1 and is part of the 8th unit cell (i.e., $n^* = 8$). The main panel shows the eigenenergies as a function of the normalized eigenstate index. The energy spectrum features two nearly continuous energy bands, five states in the band gap with energy equal to or close to zero (the state with energy exactly equal to zero is a dark state), one nontopological bound state below the bottom of the lower energy band, and one nontopological bound state above the top of the upper energy band. Insets: [(a), (b)] The eigenstates of the two nontopological bound states are shown in the upper left and upper right insets; they have energy $\pm 3.516u$. (c) The edge state shown in the lower left inset has an energy of $-4.56 \times 10^{-5}u$. (d) The dark state shown in the lower right inset has an energy of zero. The first and second SSH chains are chosen to lie along the x and y axes (the axes are chosen arbitrarily). As in Fig. 2, positive and negative expansion coefficients are shown by blue and red circles, respectively, with the size of the circles being proportional to the square of the expansion coefficients. As opposed to offsetting the sites that belong to sublattices 1 and 2 (as in Fig. 2), the lighter blue and lighter red colors correspond to sites that belong to sublattice 1 while the darker blue and darker red colors correspond to sites that belong to sublattice 2. Note the different scales of the axes of the insets.

the energy of the two-chain system with open BCs as a function of the normalized state index for $N = 15$ and $v/u = 2$. Since the two chains share one cavity, the total number of sites of the two-chain system is $4N - 1$ (recall, N refers to the number of unit cells of one of the SSH chains). As expected, the energy spectrum consists of two nearly continuous energy bands that are separated by an energy gap, which supports states with energy close to zero. The number of states in the gap is not four, as might be expected naively by doubling the number of edge states supported by the one-chain system, but five. Four states have finite energy and one state has vanishing energy. The latter is a delocalized dark state (see Appendix A), which has nonvanishing amplitude in both sublattices (see the

lower right inset of Fig. 6). An analogous nontopological dark state also exists for the two-chain system with periodic BCs but does not exist for the emitter-shared two-chain systems with periodic and open BCs. The other four states with energy close to zero can be divided into two pairs. The states belonging to the first pair, with energy $\pm\epsilon$, are approximately unaffected when g is turned on. The states belonging to the second pair with energy $\pm E_{\text{edge}}$ (see the lower left inset of Fig. 6 for an example) couple to the emitter and form, together with the state $|\text{vac}; e\rangle$, the basis for a three-state model (the same three-state Hamiltonian matrix as discussed above for the one-chain system, but with G replaced by $G/\sqrt{2}$; see Appendix D).

For comparison, the cavity-shared three-chain system with open BCs ($6N - 2$ sites with one cavity shared by all three chains) supports two dark states for $g = 0$ whose energy is exactly zero as well as another six states that also reside in the energy gap. The existence of these six states might be expected based on the naive argument that the number of edge states supported by the one-chain system triples for the three-chain system. The six states can be divided into two groups: four states that have energy $\pm\epsilon$ (two states with positive energy and two states with negative energy) and two states that have energy $\pm E_{\text{edge}}$. The latter two states couple to the emitter when g is finite and are described well by the three-state Hamiltonian matrix $\underline{H}_{\text{3-st.}}(G/\sqrt{3})$ (see Appendix D).

The energy spectrum for the cavity-shared two-chain system shown in Fig. 6 features one energy state below the bottom of the lower band and one energy state above the top of the upper band. These states have no analog in the one-chain system or the emitter-shared two- and three-chain systems and can, since they reside outside the nearly continuous energy bands, be interpreted as bound states. This interpretation is consistent with the observation that the corresponding eigenstates, which are shown in the upper left and upper right insets of Fig. 6, are localized in the vicinity of the cavity that is shared by the two SSH chains. The eigenstate that sits below the bottom of the lower band is nodeless (upper left inset of Fig. 6) while the eigenstate that sits above the top of the upper band is highly oscillatory; i.e., the eigenstate's expansion coefficients corresponding to neighboring cavities have opposite signs (upper right inset of Fig. 6). These localized bound states are nontopological in nature since they have nonvanishing population in both sublattices and also exist for $u/v = 1$ (for this ratio, the energy gap of $\hat{H}_{\text{SSH}}$ closes) as well as periodic BCs. The binding energy, measured from the bottom or top of the energy band, increases—for fixed N—with increasing number of chains.

As already alluded to, for finite g/u and $|\hbar\omega_e/u| \ll 1$, the emitter state $|\text{vac}; e\rangle$ has appreciable overlap with only three of the eigenstates that are located in the energy gap of the cavity-shared two- and three-chain systems. Dashed and dotted lines in Fig. 4 show the energy of the three states in the gap that have finite overlap with $|e; \text{vac}\rangle$ (top row) and the square of the overlap (bottom row) for, respectively, the cavity-shared two- and three-chain systems with open BCs as a function of $\hbar\omega_e$ for four different g/u values. The behavior of the gap states and their energies for the two- and three-chain systems is similar to that for the one-chain system, with the main feature that the avoided crossings are becoming somewhat narrower

as the number of chains increases from one to two and again from two to three. The observed behavior is consistent with the decrease of the effective coupling constant G by factors of $1/\sqrt{2}$ and $1/\sqrt{3}$ for the cavity-shared two-chain and three-chain systems, respectively, relative to the one-chain system with effective coupling constant G (see Appendix D). Since the three-state model applies, the hybridization discussed in the previous section carries over, with the basis states being those introduced in Appendix D. The quantity $\sum_{l=1}^{3}\mathcal{O}_l$ is greater than 0.998 for all cavity-shared two- and three-chain systems considered in Fig. 4. This is similar to what was discussed above for the corresponding emitter-shared two- and three-chain systems.

III. RESPONSE TO DISORDER

To analyze the robustness of the topological characteristics, we introduce uniformly distributed on-site disorder of the photonic part of the Hamiltonian. The disorder strengths ϵ_n are chosen from the disorder strength window $[-\Delta, \Delta]$. In the absence of the coupling to the emitter, the on-site disorder breaks the chiral symmetry of the SSH part of the Hamiltonian; hopping disorder (not considered), in contrast, preserves the chiral symmetry of the SSH part of the Hamiltonian [36]. We diagonalize the full system Hamiltonian for a large number of on-site disorder realizations and analyze, for each disorder realization, the three eigenstates $|\psi_{l'}^{\text{gap,disorder}}\rangle$ that have the largest overlap with the gap states $|\psi_l^{\text{gap}}\rangle$ for the same g/u, $\hbar\omega_e/u$, v/u, and n^* in the absence of disorder (recall that the three gap states are defined as the states that have energy close to zero and depend, for $\hbar\omega_e \neq 0$, on the value of g/u). When the disorder strength Δ/u is small, the overlap criterion employed to identify the states $|\psi_{l'}^{\text{gap,disorder}}\rangle$ is—since the largest overlap is pretty close to 1—"clean." For larger Δ/u, in contrast, the eigenstates $|\psi_{l'}^{\text{gap,disorder}}\rangle$ are found to deviate notably from the disorder-free gap states $|\psi_l^{\text{gap}}\rangle$; despite this, the largest overlap, while notably smaller than one, allows for an "unambiguous" identification of the states $|\psi_{l'}^{\text{gap,disorder}}\rangle$. The decrease of the overlap with increasing Δ/u signals that the system characteristics are fundamentally altered when the on-site disorder strength is increased.

To quantify the degree of localization of the three eigenstates $|\psi_{l'}^{\text{gap,disorder}}\rangle$, we calculate the inverse participation ratio (IPR) [27],

$$\text{IPR} = \frac{\sum_{m=1}^{M}\left|c_m^{(l')}\right|^4}{\left|\sum_{m=1}^{M}\left|c_m^{(l')}\right|^2\right|^2}, \tag{15}$$

where the expansion coefficients $c_m^{(l')}$ are given by the overlap of the state $|\psi_{l'}^{\text{gap,disorder}}\rangle$ and the mth site basis state, and M is equal to $kN - k + 2$ and $kN + 1$ for the cavity- and emitter-shared cases, respectively (in this context, the state $|\text{vac}; e\rangle$ is counted as one of the site basis states). The IPR is a measure of localization: IPRs of 1 and 0 indicate maximal and minimal localization, respectively. In addition, we analyze the polarization; i.e., we monitor if the states $|\psi_{l'}^{\text{gap,disorder}}\rangle$ occupy just one sublattice or both sublattices in each of the $2k$ arms of the k-chain systems. The IPR (see Fig. 7) together with the
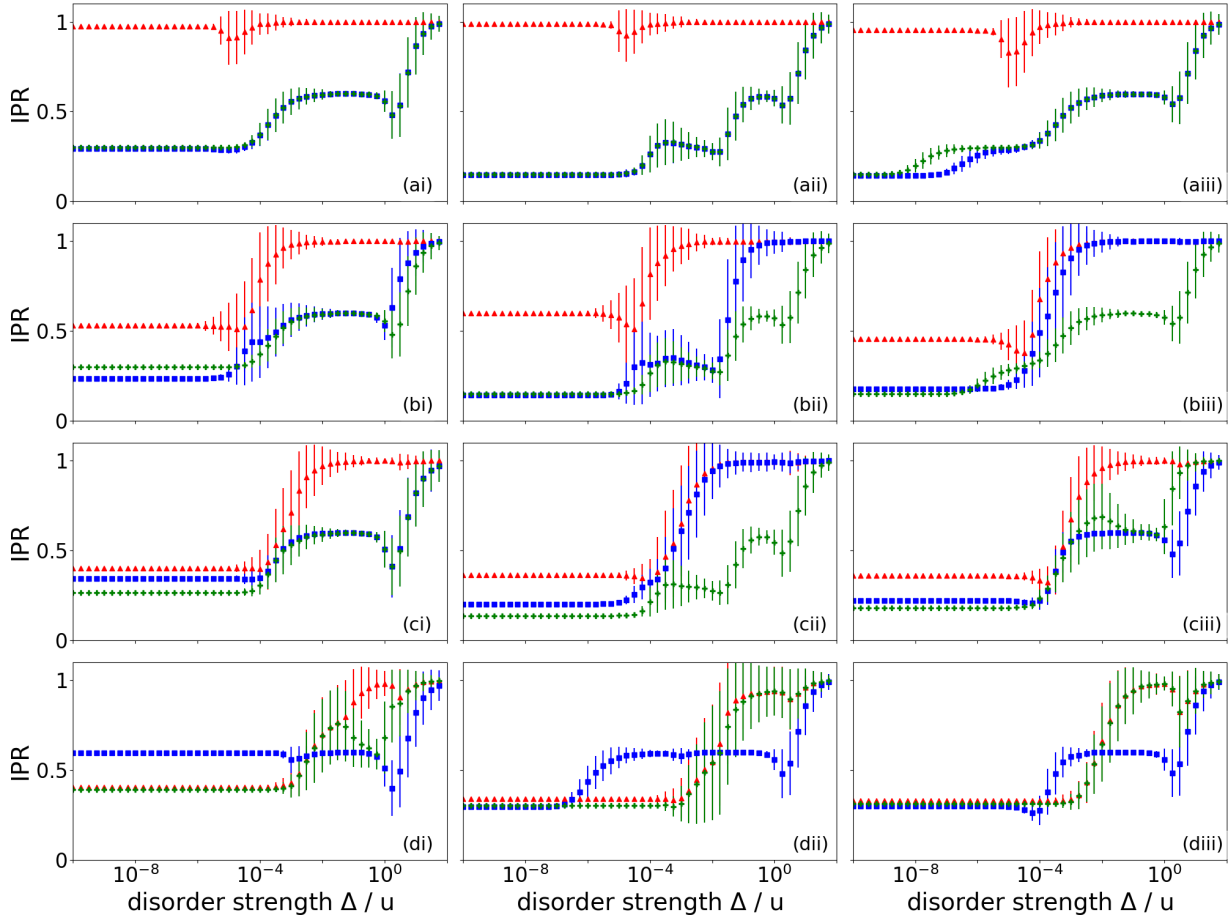
FIG. 7. IPR [see Eq. (15)] for uniformly distributed on-site disorder as a function of Δ/u (this quantity defines the scaled disorder strength window) for $\hbar\omega_e/u = -5\times10^{-5}$, $N = 15$, $v/u = 2$, $n^* = 8$, open BCs, and [(ai)–(aiii)] $g/u = 10^{-4}$, [(bi)–(biii)] $g/u = 10^{-3}$, [(ci)–(ciii)] $g/u = 10^{-2}$, and [(di)–(diii)] $g/u = 10^{-1}$. The left, middle, and right columns are for the one-chain, cavity-shared two-chain, and emitter-shared two-chain systems, respectively. The IPR is calculated for the three eigenstates of the system with disorder that have the largest overlap with the gap states of the corresponding disorder-free system. The symbols and error bars are obtained by averaging over 5×10^3 disorder realizations. In panels (ai) and (aii) as well as in parts of panels (bi) and (ci), the blue and green symbols are essentially indistinguishable. In the large-disorder regime of panels (dii) and (diii), the green and red symbols are essentially indistinguishable.

polarization (not shown) quantify the robustness of the gap state characteristics against disorder.

Symbols in Fig. 7 show the IPR for the three states $|\psi_{l'}^{\text{gap,disorder}}\rangle$ for chain systems with open BCs for $v/u = 2$, $\hbar\omega_e/u = -5\times10^{-5}$, $N = 15$, $n^* = 8$, and g/u values ranging from 10^{-4} [Figs. 7(ai)–7(aiii)] to 10^{-1} [Figs. 7(di)–7(diii)] as a function of Δ/u. The scaled disorder strength Δ/u is shown on a logarithmic scale, which covers 12 orders of magnitude; for each disorder strength, the IPR (symbols) and error bars are calculated by averaging 5×10^3 independent disorder realizations. The colors employed in Fig. 7 are "matched" with those in Fig. 4; i.e., the IPRs shown in red, blue, and green coincide—in the zero-disorder limit—with those for the states $|\psi_{l'}^{\text{gap,disorder}}\rangle$ whose energies and overlap squares are shown in red, blue, and green in Fig. 4. The left, middle, and right columns are for the one-chain system, the cavity-shared two-chain system, and the emitter-shared two-chain system, respectively. It can be seen that the changes of the IPRs and the IPRs' error bars with disorder strength depend on both

the chain geometry and the coupling strength g/u. The IPR tends to change in nontrivial ways with the disorder strength, suggesting that the disorder modifies the states $|\psi_{l'}^{\text{gap,disorder}}\rangle$ in ways that depend intricately on the energy scales of the system.

Complementing the IPR, Fig. 8 shows the distribution of the eigenenergies, averaged also over 5×10^3 disorder realizations, as a function of the scaled disorder strength Δ/u. The layout of Fig. 8 is the same as that of Fig. 7, i.e., the two figures cover the same range of scaled disorder strengths, chain geometries, and coupling strengths g/u. For each g/u, the chosen energy window (range of the y axes) in Fig. 8 is the same as in Fig. 4. Contrary to Fig. 4, Fig. 8 includes not only the energy of the gap states but of all eigenenergies that fall into the energy window. To connect the energy distribution in the band gap with the nearly continuous energy bands, Fig. 9 shows the distribution of eigenenergies of the cavity-shared two-chain system for a much larger energy window and somewhat smaller range of disorder strengths. The gap
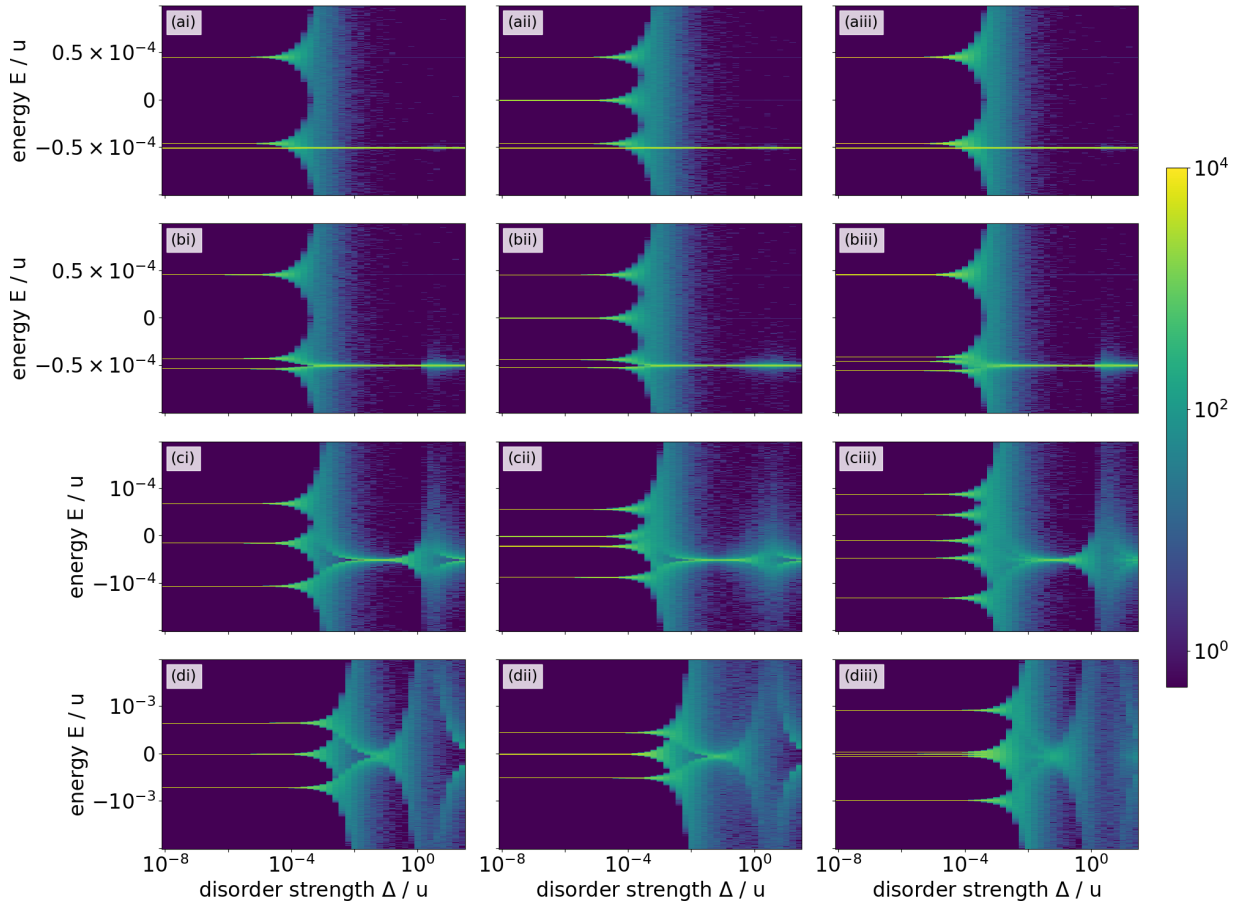
FIG. 8. Frequency of energy, color coded via the scale shown on the far right, for uniformly distributed on-site disorder (each panel uses 5×10^3 disorder realizations) as a function of Δ/u for $\hbar\omega_e/u = -5 \times 10^{-5}$, $N = 15$, $v/u = 2$, $n^* = 8$, open BCs, and [(ai)–(aiii)] $g/u = 10^{-4}$, [(bi)–(biii)] $g/u = 10^{-3}$, [(ci)–(ciii)] $g/u = 10^{-2}$, and [(di)–(diii)] $g/u = 10^{-1}$. The left, middle, and right columns are for the one-chain, cavity-shared two-chain, and emitter-shared two-chain systems, respectively.

regime, which is the focus of Fig. 8, is not resolved on this scale. Plots (not shown) for the other chain geometries and coupling strengths g/u considered in this work look essentially identical to Fig. 9, with the exception of the bound states below and above the energy bands, which only exist for the cavity-shared k-chain systems ($k \geqslant 2$; see Fig. 6).
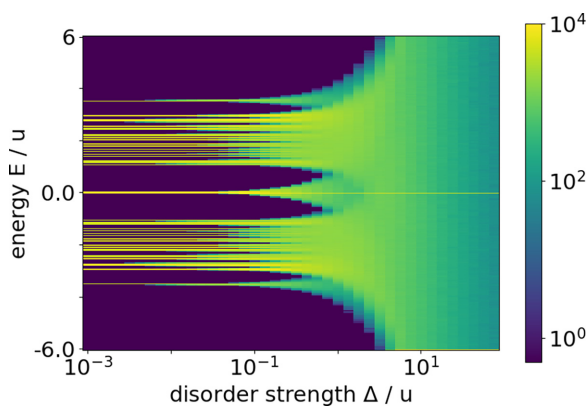

FIG. 9. Same as Fig. 8(bii), but focusing on a smaller range of disorder strengths and a larger energy window.

Combining Figs. 8 and 9, three regimes can be identified.

(i) For small Δ/u ($\Delta/u \lesssim 10^{-4}$), the energies in the gap are robust to disorder; i.e., the energies in the gap are distinguishable from each other.

(ii) For intermediate Δ/u ($10^{-4} \lesssim \Delta/u \lesssim 1$), the energies that used to lie in the gap form a band that is separated from the two nearly continuous energy bands; also, the bound states are separated from the two nearly continuous energy bands.

(iii) At large detunings ($\Delta/u \gtrsim 1$), the bands are essentially "melted" entirely; we emphasize that there exists a state with energy $\approx \hbar\omega_e$ for small g/u and large Δ/u that is only minimally impacted by the disorder.

Importantly, we find that the population in a given arm of the k-chain systems is, for all gap states $|\psi_{l'}^{\text{gap,disorder}}\rangle$, to a very good approximation either located in sublattice 1 or in sublattice 2 up to disorder strength $\Delta/u \approx 10^{-3}$ [this includes regime (i) as well as a portion of regime (ii) introduced above]; i.e., the topological characteristic of population being localized on only one sublattice in a given arm is preserved up to a critical disorder strength that depends relatively weakly on the coupling strength and chain geometry and is about 20 times larger than $|E_{\text{edge}}|$.

We now discuss selected limits. We start with the $\Delta/u \to 0$ limit (arbitrary g/u). Appendixes B and C show that the IPRs

for the one-chain and emitter-shared two-chain system for $\Delta/u = 0$ are reproduced with high accuracy (at the percent level or better) by the analytical three-state model expressions [see Eqs. (B10) and (C8)] for all g/u considered in Fig. 7. Notably, to approach the zero-disorder limit for the emitter-shared two-chain system with $g/u = 10^{-4}$ [Fig. 7(aiii)], the scaled disorder strength must be smaller than 10^{-8}, i.e., more than three orders of magnitude smaller than $\hbar\omega_e/u$, g/u, and $|E_{\text{edge}}|/u$. For the one-chain and cavity-shared two-chain system, in contrast, Δ/u must be $\lesssim 10^{-5}$ for the zero-disorder limit to be approached.

Next, we consider the small-(g/u) limit [see Figs. 7(ai)–7(aiii) and Figs. 8(ai)–8(aiii)]. For the smallest g/u considered (namely, $g/u = 10^{-4}$), the IPR for the state $|\psi_{l'}^{\text{gap,disorder}}\rangle$ that is dominated by the basis state $|\text{vac}; e\rangle$ is very close to 1 for all disorder strengths [red triangles in Figs. 7(ai)–7(aiii)]. The error bar is small for small Δ/u, then increases, and is small again for Δ/u larger than 10^{-3}. In the latter regime, the state has an energy close to $\hbar\omega_e$ [yellowish stripe in Figs. 8(ai)–8(aiii)] and is localized at the emitter. Scaled disorders around 10^{-3} lead—for $g/u = 10^{-4}$—to state localization and the re-opening of an energy gap. At very strong disorder, the IPRs of the other two states [shown in green and blue in Figs. 7(ai)–7(aiii)] also approach 1, signaling Anderson localization [37]; this behavior is reminiscent of what was observed in Ref. [27]. We note that most of the energies of these states lie outside of the energy windows shown in Figs. 8(ai)–8(aiii).

For the emitter-shared two-chain system, a very weak disorder leads for $|G/E_{\text{edge}}| \ll 1$ to a change of one of the states with edgelike character [green symbols in Fig. 7(aiii)]: the state changes from having population in all four arms to having population in only two arms, which may belong to the same chain or different chains. For the cavity-shared two-chain system, a weak disorder leads for $|G/E_{\text{edge}}| \gg 1$ to a distinct change of the IPR shown by blue symbols in Fig. 7(dii): the state changes from being localized in two arms to being localized in one arm. These examples illustrate that the response of the states that live in the gap to on-site disorder depends sensitively on how the SSH chains are connected to each other (through a cavity or through an emitter). In particular, very weak disorder can lead to distinct differences in the system response of the cavity-shared and emitter-shared k-chain systems in a regime where the disorder modifies the eigenenergies extremely weakly. This can be understood by realizing that the disorder breaks the discrete rotation symmetry associated with the k-chain systems (invariance of the Hamiltonian under exchange of any two chain indices for $k \geqslant 2$), favoring—in some cases—states that localize on one chain as opposed to populating all k chains equally.

IV. TIME-DEPENDENT SIGNATURE OF THE HYBRIDIZATION

This section shows that the transition from the excited emitter state contributing predominantly to one state to contributing predominantly to two states in k-chain systems with open BCs can be probed dynamically (see also Ref. [12]). Figure 10 shows the population dynamics of the one-chain system [Figs. 10(a) and 10(c)] and cavity-shared two-chain system [Figs. 10(b) and 10(d)] as a function of the site basis
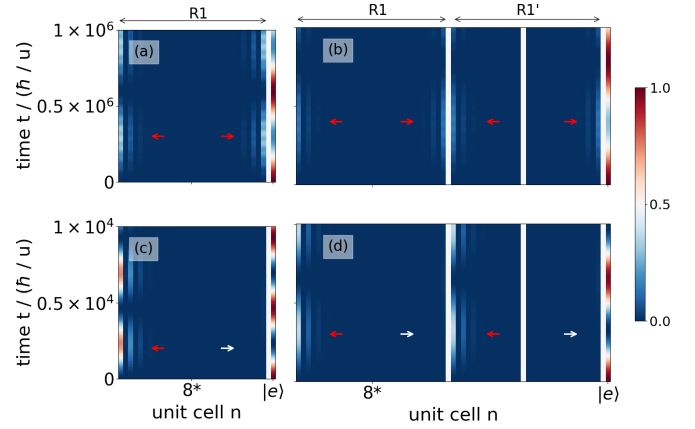

FIG. 10. Population dynamics of the [(a), (c)] one-chain system and [(b), (d)] cavity-shared two-chain system with $N = 15$, $v/u = 2$, $n^* = 8$, $\hbar\omega_e/u = -5\times10^{-5}$, and open BCs. The populations of the site basis states $|n, j; \sigma\rangle$ (first chain of one- and two-chain systems) and $|n', j; \sigma\rangle$ (second chain of two-chain system) are shown as a function of time; the color bar shown on the right applies to all panels. The top and bottom rows are for $g/u = 10^{-3}$ and $g/u = 10^{-1}$, respectively. For the one-chain system, the order of the basis states from left to right is $|1, 1; g\rangle$, $|1, 2; g\rangle$, ..., $|N, 1; g\rangle$, $|N, 2; g\rangle$, and $|\text{vac}; e\rangle$; the "white stripe" immediately to the left of the last basis state visually separates the basis states where the emitter is in $|g\rangle$ from those where the emitter is in $|e\rangle$. For the two-chain system, the order of the basis states from left to right is $|1, 1; g\rangle$, ..., $|N, 2; g\rangle$, $|1', 1; g\rangle$, ..., $|N', 2; g\rangle$, and $|\text{vac}; e\rangle$; the first, second, and third "white stripes" (from left to right) visually separate the basis states belonging to the first and second chain, mark the sublattice 1 cavity of the second chain that is "missing" from the second chain (due to it being shared with the first chain), and separate basis states where the emitter is in $|g\rangle$ from those where the emitter is in $|e\rangle$, respectively. The red and white arrows highlight the presence and absence, respectively, of population in the cavities located at the ends of the chains.

for $\hbar\omega_e/u = -5\times10^{-5}$ and two different g/u values, namely, $g/u = 10^{-3}$ (top row) and $g/u = 10^{-1}$ (bottom row). The basis state in which the emitter is excited (namely, basis state $|\text{vac}; e\rangle$) is placed on the far right. The other basis states are ordered to alternate between sublattice 1 and sublattice 2. For the one-chain system, the unit cell index n increases from left to right. For the two-chain system, the $2N$ basis states (emitter in $|g\rangle$ and unit cell index n) of the first chain are shown first, followed by the $2N - 1$ basis states (emitter in $|g\rangle$ and unit cell index n') of the second chain.

We first consider the dynamics of the one-chain system. The excited emitter state $|\text{vac}; e\rangle$ has a population of 1 at $t = 0$ and then oscillates with a frequency that can be obtained analytically using the three-state model introduced in Sec. II B. Interestingly, while the dynamics of the population of state $|\text{vac}; e\rangle$ is qualitatively similar for the two g/u values considered, albeit with different oscillation frequency, the population dynamics of the states $|n, j; g\rangle$ shows a marked difference for the two different g values. For $g/u = 10^{-3}$, both end cavities of the chain have an enhanced population when the population of the state $|\text{vac}; e\rangle$ is smallest [see red arrows in Fig. 10(a)]. For $g/u = 10^{-1}$, in contrast, the left end of the chain displays

an enhanced population while the right end of the chain does not [white arrow in Fig. 10(c)]. These population dynamics are consistent with our discussion in the previous section and, in particular, with our conclusion that the excited emitter state hybridizes with the photonic components that live on the left arm of the chain for $g/u \gtrsim 10^{-2}$. The initial state has essentially zero overlap with the gap state that has approximately zero energy [see blue solid lines in Figs. 2(d) and 2(h)] and can be, in the large-G limit, approximated by $|\psi_{edge,R}; g\rangle$ (see Sec. II B and Appendix B). As a consequence, the absence of population in the right arm, marked by the white arrow in Fig. 10(c), can be interpreted as a key fingerprint of the change of the hybridization of the gap states for sufficiently large G. If we repeat the dynamical study for $\hbar\omega_e = 0$ but otherwise identical parameters (not shown), we find that the photonic populations on the right arm undergo oscillations for $g/u = 10^{-3}$ (the left arm has vanishing photonic populations) and those on the left arm undergo oscillations for $g/u = 10^{-1}$ (the right arm has vanishing photonic populations); see the insets of Fig. 5 for depictions of the corresponding $\hbar\omega_e = 0$ gap states.

The dynamics of the cavity-shared two-chain system is analogous to that of the one-chain system, with the dynamics of the two-chain system being slightly slower than that of the one-chain system, as would be expected based on the small but visible changes of the energy spectra with the number of chains (see the top row of Fig. 4). For $g/u = 10^{-3}$, the population of the four end cavities is maximal when the population of the state $|vac; e\rangle$ is minimal [red arrows in Fig. 10(b)]. For $g/u = 10^{-1}$, in contrast, only the left ends of both chains get populated appreciably [red and white arrows in Fig. 10(d)]. As in the one-chain case, the excited emitter state hybridizes with the $g = 0$ edge states such that, for sufficiently strong coupling, only cavities in the left arms of the chains are occupied. In analogy to the one-chain case, the absence of population in two arms for sufficiently large G [white arrows in Fig. 10(d)] signals the change in hybridization. The behavior for the cavity-shared three-chain system with open BCs (not shown) is similar to that for the one-chain and cavity-shared two-chain systems with open BCs.

V. CONCLUSIONS

This work investigated static and dynamic properties of one, two, and three SSH chains, which possess chiral symmetry, coupled weakly to a 2LE that breaks the chiral symmetry. In the case of a single chain, the emitter was coupled to one of the lattice sites. In the case of the two- and three-chain systems, the emitter was either coupled to one lattice site of each chain (emitter-coupled k-chain system; $k = 2$ or 3) or to a single lattice site that was shared between the chains (cavity-coupled k-chain system). Since the rotating wave approximation was employed, coupling strengths were limited to $g/u \leqslant 10^{-1}$. Using open BCs and working in the single-excitation manifold, this work focused on the states that reside in the energy gap between the two nearly continuous energy bands. Throughout, the excitation energy of the emitter was chosen such that the emitter was in resonance with the band gap. The number of states in the band was found to depend on the chain geometry. For all chain geometries considered,

it was found that the eigenstates in the gap could be grouped into three states that depend on the coupling strength g/u and zero or more states that, to a very good approximation, had zero population in the emitter. A fully analytical three-state model was found to provide an excellent description of the g-dependent gap states with topological characteristics for all k-chain systems investigated.

This work exploited that a SSH chain with open BCs is characterized by a finite edge state energy E_{edge}, leading to a g-dependent hybridization that is absent in the system with periodic BCs. This finite energy scale modifies the role of the emitter from being perturbative for $|G/E_{edge}| \lesssim 1$ to being nonperturbative for $|G/E_{edge}| \gtrsim 1$. The hybridization of the excited emitter state and the $g = 0$ edge states was analyzed in detail and the behavior was contrasted with that for the system with periodic BCs.

Generalizations and variants of the paradigmatic SSH model include studies of two nonreciprocal coupled SSH chains [38], a bipartite lattice of domain wall states [39], and topological synchronization [40]. Our work adds to the growing body of emitters coupled to topological waveguides [12,15,41,42]. Extensions of the present work to three-level emitters, which themselves support dark states, will open the door for coupling the dark state of the emitter and the dark states of cavity-coupled k-chain systems. In hyperbolic lattices, which contain chain- or ringlike building blocks, the relaxation dynamics of a 2LE was recently proposed as a probe of the hyperbolic bath [43]. Another intriguing prospect is to work in the weak-coupling regime where the emitter plays a perturbative role and to devise sensing protocols by which the emitter dynamics, or that of two entangled emitters, can be used to probe topological matter.

APPENDIX A: DARK STATES

This Appendix determines the number of dark states, i.e., the number of eigenstates of $\hat{H}_{Ck\text{-}2LE}$ that have vanishing energy. The cavity-shared k-chain system in the single-excitation subspace is spanned by a total of $(kN - k + 1) + (kN) + 1 = 2kN - k + 2$ basis states. It proves useful to reorder the site basis states as follows: the basis states $1, \ldots, kN - k + 1$ are of type $|n, 1; g\rangle$; the basis states $kN - k + 2, \ldots, 2kN - k + 1$ are of type $|n, 2; g\rangle$ (there are kN basis states of this type); and the basis state $2kN - k + 2$ is equal to $|vac; e\rangle$. With this ordering, the Hamiltonian matrix $\underline{H}_{Ck\text{-}2LE}$ has the simple block structure

$$\underline{H}_{Ck\text{-}2LE} = \begin{pmatrix} \underline{O} & \underline{V} \\ \underline{V}^\dagger & \underline{P} \end{pmatrix}, \tag{A1}$$

where $\underline{O}$, $\underline{P}$, and $\underline{V}$ are matrices of size $(kN - k + 1) \times (kN - k + 1)$, $(kN + 1) \times (kN + 1)$, and $(kN + 1) \times (kN - k + 1)$, respectively. The matrix elements of $\underline{O}$ are all equal to zero since $\hat{H}_{Ck\text{-}2LE}$ does not couple basis states $|n, 1; g\rangle$ and $|n', 1; g\rangle$ for either $n = n'$ or $n \neq n'$. The

square matrix $\underline{P}$ arises from combining the states $|n, 2; g\rangle$ and $|\text{vac}; e\rangle$. The matrix elements of $\underline{P}$ are all equal to zero, except for the element $P_{2kN-k+2,2kN-k+2}$, which is equal to $\hbar\omega_e$. A key point is that the basis states are ordered such that the matrix $\underline{V}$ accounts for all "couplings"; i.e., the Hamiltonian terms proportional to u, v, v_N, and g are included in $\underline{V}$. Note in particular that, since the emitter is not coupled to sublattice 2 but to sublattice 1, the coupling constant g does not enter into $\underline{P}$ (i.e., $\underline{P}$ contains at most one nonzero entry).

To proceed, we first consider the special case where the detuning $\hbar\omega_e$ is equal to zero. In this case, all matrix elements of $\underline{P}$ are equal to zero. Applying the results from the Appendix of Ref. [44], it follows that the number of dark states is given by the difference, in magnitude, between the number of rows and the number of columns of $\underline{V}$. The cavity Hamiltonian $\hat{H}_{Ck\text{-}2\text{LE}}$ hence supports k dark states for $\hbar\omega_e = 0$. For $\hbar\omega_e \neq 0$, one of the dark states turns "bright"; i.e., the energy of this state is pushed away from zero. This behavior is clearly visible in the top row of Fig. 4. Mathematically, the disappearance of the dark state follows since the right lower matrix element of $\underline{P}$ takes on a finite value. To summarize, the cavity-coupled k-chain systems with $\hbar\omega_e \neq 0$ support $k - 1$ dark states (see Fig. 3).

The arguments for determining the number of dark states for the emitter-shared k-chain systems proceed analogously. Keeping the same grouping of the basis states, the matrices $\underline{O}$, $\underline{P}$, and $\underline{V}$ are of size $(kN)\times(kN)$, $(kN + 1)\times(kN + 1)$, and $(kN + 1)\times(kN)$, respectively. The key difference compared to the cavity-shared systems is that the number of basis states of type $|n, 1; g\rangle$ is kN in the emitter-shared system as opposed to $kN - k + 1$. Applying the results from the Appendix of Ref. [44], it follows that the emitter-shared k-chain systems support exactly one dark state if and only if $\hbar\omega_e = 0$. Figure 3 indicates the absence of dark states since it summarizes the more general $\hbar\omega_e \neq 0$ case (the special $\hbar\omega_e = 0$ case is referred to in the caption).

APPENDIX B: THREE-STATE MODEL FOR GAP STATES OF ONE-CHAIN SYSTEM

Section II B discusses selected properties of the three-state Hamiltonian $\underline{H}_{3\text{-st.}}(G)$. This Appendix presents analytical expressions for three special cases. The eigenvalues of $\underline{H}_{3\text{-st.}}(G)$ can be obtained by solving the cubic equation

$$\lambda^3 - \hbar\omega_e\lambda^2 - [2G^2 + (E_{\text{edge}})^2]\lambda + \hbar\omega_e(E_{\text{edge}})^2 = 0. \quad (B1)$$

Special case 1. When the detuning vanishes, the eigenenergies are equal to

$$\lambda|_{\hbar\omega_e=0} = 0 \quad (B2)$$

and

$$\lambda|_{\hbar\omega_e=0} = \pm[2G^2 + (E_{\text{edge}})^2]^{1/2}. \quad (B3)$$

This shows that the splitting between the energetically lowest- and highest-lying gap states is approximately equal to $2|E_{\text{edge}}|$ and $2\sqrt{2}G$ when $2G^2 \ll (E_{\text{edge}})^2$ and $2G^2 \gg (E_{\text{edge}})^2$, respectively. These inequalities suggest that a "transition" occurs when $\sqrt{2}G$ is comparable to $|E_{\text{edge}}|$. The unnormalized zero-energy eigenstate reads $(G/E_{\text{edge}}, -G/E_{\text{edge}}, 1)$.

Special case 2. Figure 4 shows that the energy levels undergo two separate avoided crossings when g/u is small [Figs. 4(a) and 4(b)]. When g/u is comparatively large [Fig. 4(d)], in contrast, the two avoided crossings can no longer be treated separately. To identify the energy scale at which the crossings start to overlap, we consider a two-state model, which removes the first row and first column from $\underline{H}_{3\text{-st.}}(G)$. The eigenenergies $\lambda_{2\text{-st.}}$ of the two-state model are given by

$$\lambda_{2\text{-st.}} = \frac{\hbar\omega_e + E_{\text{edge}}}{2} \pm \sqrt{\left(\frac{\hbar\omega_e - E_{\text{edge}}}{2}\right)^2 + G^2} \quad (B4)$$

and the energy splitting at the avoided crossing is equal to $2G$. Since the energies of these two states have the same magnitude but opposite sign, it is readily argued from this splitting that the two avoided crossings can no longer be treated separately if $2G$ approaches $|E_{\text{edge}}|$. As expected, the "competition scale" obtained via the two-state model is similar to that obtained from the three-state model. For the data shown in Fig. 4, the competition scale is reached roughly when g/u is equal to 10^{-2}, consistent with what is concluded by visual inspection.

Special case 3. To gain additional insight into the larger g/u regime [Fig. 4(d)], we return to the three-state model and consider the limit where $|E_{\text{edge}}|$ is much smaller than G. Setting $E_{\text{edge}} = 0$, the eigenvalues of $\underline{H}_{3\text{-st.}}(G)$ are

$$\lambda|_{E_{\text{edge}}=0} = 0 \quad (B5)$$

and

$$\lambda|_{E_{\text{edge}}=0} = \frac{\hbar\omega_e}{2} \pm \sqrt{\left(\frac{\hbar\omega_e}{2}\right)^2 + 2G^2}. \quad (B6)$$

The eigenstate corresponding to $\lambda|_{E_{\text{edge}}=0} = 0$ is equal to $(|\psi_+^{\text{C1}}\rangle - |\psi_-^{\text{C1}}\rangle)|g\rangle/\sqrt{2} = |\psi_{\text{edge,R}}\rangle|g\rangle$; i.e., this eigenstate has nonvanishing amplitude only in one side of the chain and only in sublattice 2 (see Sec. II B for further discussion).

Altogether, the analysis outlined in this Appendix shows that the emitter acts as a perturbation when g/u is much smaller than about $|E_{\text{edge}}/(uc_{n^*,1})|$. The state $|\text{vac}; e\rangle$ hybridizes with the $g = 0$ edge states (emitter in $|g\rangle$) when the effective coupling G is comparable to $|E_{\text{edge}}|$. Where the transition occurs can be tuned by increasing g/u for fixed N or by increasing N for fixed g/u. We note that the unit cell n^* at which the emitter is placed can also be used as a tuning knob.

We now present approximate analytical expressions for the IPR. We start with the photonic Hamiltonian (excluding the emitter Hilbert space). The IPR for the states $|\psi_\pm^{\text{C1}}\rangle$ reads

$$\text{IPR}_{|\psi_\pm^{\text{C1}}\rangle} = \frac{\mathcal{N}^2\left[1 + \left(\frac{u}{v}\right)^{2N}\right]}{2 + 2\left(\frac{u}{v}\right)^2}, \quad (B7)$$

which can be simplified to

$$\text{IPR}_{|\psi_\pm^{\text{C1}}\rangle} \approx \frac{1 - \left(\frac{u}{v}\right)^2}{2 + 2\left(\frac{u}{v}\right)^2}. \quad (B8)$$

For $u/v = 2$ and $N = 15$, e.g., Eq. (B8) evaluates to $3/10$, which deviates from Eq. (B7) by less than 6×10^{-10}.

To obtain approximate analytical expressions for the IPR for the states $|\psi_l^{\text{gap}}\rangle$ (one-chain system with finite g), we write

$$\left|\psi_l^{\text{gap}}\right\rangle = d_+^{(l)}|\psi_+^{C1}\rangle|g\rangle + d_-^{(l)}|\psi_-^{C1}\rangle|g\rangle + d_e^{(l)}|\text{vac}, e\rangle, \quad (B9)$$

where the expansion coefficients $d_+^{(l)}$, $d_-^{(l)}$, and $d_e^{(l)}$ are extracted from the eigenvectors of the three-state model. Evaluating the IPR for the states given in Eq. (B9), we find

$$\text{IPR}_{|\psi_l^{\text{gap}}\rangle} = \text{IPR}_{|\psi_\pm^{C1}\rangle}(|d_+^{(l)}|^4 + |d_-^{(l)}|^4 + 6|d_+^{(l)}|^2|d_-^{(l)}|^2) + \left|d_e^{(l)}\right|^4. \quad (B10)$$

APPENDIX C: EMITTER-SHARED TWO- AND THREE-CHAIN SYSTEMS

To construct a few-state model that describes the g dependence of the energy levels that lie in the middle of the gap for $k > 1$, we first consider the emitter-shared two-chain system. We introduce approximate expressions for the $g = 0$ eigenstates with energy close to zero. Since the two chains are decoupled for $g = 0$, the system supports two eigenstates with energy E_{edge} and two eigenstates with energy $-E_{\text{edge}}$,

$$|\psi_\pm^{C1}\rangle|\text{vac}, C2\rangle|g\rangle \quad (C1)$$

and

$$|\text{vac}, C1\rangle|\psi_\pm^{C2}\rangle|g\rangle, \quad (C2)$$

where $|\text{vac}, Ck\rangle$ refers to the vacuum state of chain k and where the state $|\psi_\pm^{C2}\rangle$ is defined analogously to $|\psi_\pm^{C1}\rangle$ (see Sec. II B). To construct a few-state model, we form linear combinations of the two states that have energy E_{edge} as well as linear combinations of the two states that have energy $-E_{\text{edge}}$:

$$\frac{1}{\sqrt{2}}(|\psi_+^{C1}\rangle|\text{vac}, C2\rangle \pm |\text{vac}, C1\rangle|\psi_+^{C2}\rangle)|g\rangle \quad (C3)$$

and

$$\frac{1}{\sqrt{2}}(|\psi_-^{C1}\rangle|\text{vac}, C2\rangle \pm |\text{vac}, C1\rangle|\psi_-^{C2}\rangle)|g\rangle. \quad (C4)$$

The "+"-linear combinations couple to the state $|\text{vac}, C1\rangle|\text{vac}, C2\rangle|e\rangle$ while the "−"-linear combinations do not. Correspondingly, we consider a three-state model that is spanned by the two "+"-linear combinations and $|\text{vac}, C1\rangle|\text{vac}, C2\rangle|e\rangle$. Calculating the coupling matrix elements, we find that the coupling strength is $\sqrt{2}$ times larger than that of the one-chain system; i.e., the three-state Hamiltonian is given by $\underline{H}_{\text{3-st.}}(\sqrt{2}G)$ [Eq. (13) with G replaced by $\sqrt{2}G$].

The emitter-shared three-chain system supports seven states with energy close to zero. Forming appropriate linear combinations, we find that only three of these are shifted when

g is turned on. Thus, we construct a three-state model spanned by the states

$$\frac{1}{\sqrt{3}}(|\psi_+^{C1}\rangle|\text{vac}, C2\rangle|\text{vac}, C3\rangle + |\text{vac}, C1\rangle|\psi_+^{C2}\rangle|\text{vac}, C3\rangle$$
$$+ |\text{vac}, C1\rangle|\text{vac}, C2\rangle|\psi_+^{C3}\rangle)|g\rangle, \quad (C5)$$

$$\frac{1}{\sqrt{3}}(|\psi_-^{C1}\rangle|\text{vac}, C2\rangle|\text{vac}, C3\rangle + |\text{vac}, C1\rangle|\psi_-^{C2}\rangle|\text{vac}, C3\rangle$$
$$+ |\text{vac}, C1\rangle|\text{vac}, C2\rangle|\psi_-^{C3}\rangle)|g\rangle, \quad (C6)$$

and

$$|\text{vac}, C1\rangle|\text{vac}, C2\rangle|\text{vac}, C3\rangle|e\rangle. \quad (C7)$$

The three-state Hamiltonian for the emitter-shared three-chain systems is given by $\underline{H}_{\text{3-st.}}(\sqrt{3}G)$ [Eq. (13) with G replaced by $\sqrt{3}G$]. For the emitter-shared k-chain system, the effective coupling energy is $\sqrt{k}G$.

As in the one-chain system, we can—analogously to Eq. (B9)—write the gap states $|\psi_l^{\text{gap}}\rangle$ for the emitter-shared k-chain systems as a superposition of the three states that span the three-state Hamiltonian. Evaluating the IPR within the three-state model, we find

$$\text{IPR}_{|\psi_l^{\text{gap}}\rangle}$$
$$= \frac{\text{IPR}_{|\psi_\pm^{C1}\rangle}}{j}(|d_+^{(l)}|^4 + |d_-^{(l)}|^4 + 6|d_+^{(l)}|^2|d_-^{(l)}|^2) + \left|d_e^{(l)}\right|^4, \quad (C8)$$

where $d_+^{(l)}$, $d_-^{(l)}$, and $d_e^{(l)}$ are obtained from the eigenvectors of the three-state Hamiltonian.

APPENDIX D: CAVITY-SHARED TWO- AND THREE-CHAIN SYSTEMS

For the cavity-shared k-chain systems, the $g = 0$ eigenstates with eigenenergy close to zero fall into three groups. The first group contains, for the two-chain system (three-chain system), two (four) states with energies that are finite but different from $\pm E_{\text{edge}}$ and that are, to a very good approximation, not affected when the coupling g is turned on. The second group contains one (two) nontopological dark states (see Appendix A). The third group contains three states with energies $-E_{\text{edge}}$, E_{edge}, and $\hbar\omega_e$ that couple to the emitter when g is nonzero. The states with energies $\pm E_{\text{edge}}$ are essentially identical to those introduced in Appendix C, with the exception that there only exists one basis state $|n^*, 1\rangle$ as opposed to k basis states $|n^*, 1; Ck\rangle$. Using these two states together with $|\text{vac}; e\rangle$, we find that the three-state Hamiltonian matrix for the cavity-shared systems is identical to that for the one-chain systems but with reduced coupling constant [Eq. (13) with G replaced by $G/\sqrt{k}$]. The reduction of the coupling energy compared to the one-chain and emitter-shared systems is due to the fact that the cavity that the emitter is coupled to is shared among all chains.

[1] I. Carusotto and C. Ciuti, Rev. Mod. Phys. **85**, 299 (2013).

[2] A. Reiserer and G. Rempe, Rev. Mod. Phys. **87**, 1379 (2015).

[3] P. Forn-Díaz, L. Lamata, E. Rico, J. Kono, and E. Solano, Rev. Mod. Phys. **91**, 025005 (2019).

[4] E. Janitz, M. K. Bhaskar, and L. Childress, Optica **7**, 1232 (2020).

[5] F. Schlawin, D. M. Kennes, and M. A. Sentef, Appl. Phys. Rev. **9**, 011312 (2022).

[6] S. Haroche, Rev. Mod. Phys. **85**, 1083 (2013).

[7] D. J. Wineland, Rev. Mod. Phys. **85**, 1103 (2013).

[8] F. Ciccarello, Phys. Rev. A **83**, 043802 (2011).

[9] K. Lalumière, B. C. Sanders, A. F. van Loo, A. Fedorov, A. Wallraff, and A. Blais, Phys. Rev. A **88**, 043806 (2013).

[10] H. Zheng, D. J. Gauthier, and H. U. Baranger, Phys. Rev. Lett. **111**, 090502 (2013).

[11] G. Calajó, F. Ciccarello, D. Chang, and P. Rabl, Phys. Rev. A **93**, 033833 (2016).

[12] M. Bello, G. Platero, J. I. Cirac, and A. Gonzáles-Tudela, Sci. Adv. **5**, eaaw0297 (2019).

[13] S. J. Masson and A. Asenjo-Garcia, Phys. Rev. Res. **2**, 043213 (2020).

[14] B. Kannan, M. J. Ruckriegel, D. L. Campbell, A. F. Kockum, J. Braumüller, D. K. Kim, M. Kjaergaard, P. Krantz, A. Melville, B. M. Niedzielski, A. Vepsäläinen, R. Winik, J. L. Yoder, F. Nori, T. P. Orlando, S. Gustavsson, and W. D. Oliver, Nature (London) **583**, 775 (2020).

[15] E. Kim, X. Zhang, V. S. Ferreira, J. Banker, J. K. Iverson, A. Sipahigil, M. Bello, A. González-Tudela, M. Mirhosseini, and O. Painter, Phys. Rev. X **11**, 011015 (2021).

[16] D. Petrosyan and M. Fleischhauer, Phys. Rev. Lett. **100**, 170501 (2008).

[17] F. Flamini, N. Spagnolo, and F. Sciarrino, Rep. Prog. Phys. **82**, 016001 (2019).

[18] S. Slussarenko and G. J. Pryde, Appl. Phys. Rev. **6**, 041303 (2019).

[19] J. D. Brehm, A. N. Poddubny, A. Stehli, T. Wolz, H. Rotzinger, and A. V. Ustinov, npj Quantum Mater. **6**, 10 (2021).

[20] D. Martín-Cano, A. González-Tudela, L. Martín-Moreno, F. J. García-Vidal, C. Tejedor, and E. Moreno, Phys. Rev. B **84**, 235306 (2011).

[21] I. M. Mirza and J. C. Schotland, Phys. Rev. A **94**, 012309 (2016).

[22] J. Kumlin, S. Hofferberth, and H. P. Büchler, Phys. Rev. Lett. **121**, 013601 (2018).

[23] W. P. Su, J. R. Schrieffer, and A. J. Heeger, Phys. Rev. Lett. **42**, 1698 (1979).

[24] M. Capone, W. Stephan, and M. Grilli, Phys. Rev. B **56**, 4484 (1997).

[25] E. J. Meier, F. A. An, and B. Gadway, Nat. Commun. **7**, 13986 (2016).

[26] S. Lieu, Phys. Rev. B **97**, 045106 (2018).

[27] M. Scollon and M. P. Kennett, Phys. Rev. B **101**, 144204 (2020).

[28] L. Leonforte, A. Carollo, and F. Ciccarello, Phys. Rev. Lett. **126**, 063601 (2021).

[29] V. Perebeinos, J. Tersoff, and P. Avouris, Phys. Rev. Lett. **94**, 027402 (2005).

[30] P. St-Jean, V. Goblot, E. Galopin, A. Lemaître, T. Ozawa, L. Le Gratiet, I. Sagnes, J. Bloch, and A. Arno, Nat. Photon. **11**, 651 (2017).

[31] R. Jackiw and J. R. Schrieffer, Nucl. Phys. B **190**, 253 (1981).

[32] J. K. Asbóth, L. Oroszlány, and A. Pályi, *A Short Course on Topological Insulators* (Springer, Cham, 2016).

[33] M. Z. Hasan and C. L. Kane, Rev. Mod. Phys. **82**, 3045 (2010).

[34] C.-K. Chiu, J. C. Y. Teo, A. P. Schnyder, and S. Ryu, Rev. Mod. Phys. **88**, 035005 (2016).

[35] P. Lambropoulos and D. Petrosyan, *Fundamentals of Quantum Optics and Quantum Information* (Springer, New York, 2007).

[36] M. Inui, S. A. Trugman, and E. Abrahams, Phys. Rev. B **49**, 3190 (1994).

[37] P. W. Anderson, Phys. Rev. **109**, 1492 (1958).

[38] W.-X. Cui, L. Qi, Y. Xing, S. Liu, S. Zhang, and H.-F. Wang, Opt. Express **28**, 37026 (2020).

[39] F. Munoz, F. Pinilla, J. Mella, and M. I. Molina, Sci. Rep. **8**, 17330 (2018).

[40] C. W. Wächtler and G. Platero, Phys. Rev. Res. **5**, 023021 (2023).

[41] S. Barik, A. Karasahin, C. Flower, T. Cai, H. Miyake, W. Degottardi, M. Hafezi, and E. Waks, Science **359**, 666 (2018).

[42] S. Barik, A. Karasahin, S. Mittal, E. Waks, and M. Hafezi, Phys. Rev. B **101**, 205303 (2020).

[43] P. Bienias, I. Boettcher, R. Belyansky, A. J. Kollár, and A. V. Gorshkov, Phys. Rev. Lett. **128**, 013601 (2022).

[44] P. Boross, J. K. Asbóth, G. Széchenyi, L. Oroszlány, and A. Pályi, Phys. Rev. B **100**, 045414 (2019); see also J. R. Morris and B. W. Shore, Phys. Rev. A **27**, 906 (1983).